ADVANCED ENGINEERING MATERIALS
www.aem-journal.com

Viologen Salt Bridge-Equipped Ionic Covalent Organic Polymers Directed toward Anionic Adsorption

Jerk-Sheuan Wong, Mahmoud Younis, Pei-Cih Hu, Cheng-Yeh Hsin, Hongta Yang, Po-Hsun Chen, Po-Liang Liu, Yu-En Liang, Yi-Tsu Chan, and Rong-Ho Lee**

The well-defined porosity architectures and distinct charge characteristics of ionic covalent organic polymers (ICOPs) have garnered significant attention as promising candidates for drug delivery, adsorption, separation, and gas collection and storage applications. This study reports the synthesis of two novel ICOPs, TPE-COP and PY-COP, based on tetraphenylethene and pyrene cores, respectively, with viologen serving as the conjugated bridge. To complement the experimental findings and provide microscopic insights into the adsorption mechanism, density functional theory calculations are performed. Results indicate that the PY-COP model exhibits a more planar structure compared to TPE-COP, explaining the observed morphological variations: spherical for TPE-COP and stacked morphology for PY-COP. TPE-COP exhibits markedly stronger stabilization toward oxoanions. Saturated adsorption capacities are determined for both ICOPs against selected anionic pollutants, demonstrating competitive performance compared to existing adsorbents. For $KMnO_4$, TPE-COP and PY-COP demonstrate capacities of 0.77 and 0.35 g MnO_4^- g^{-1}, respectively. Similarly, for $Na_2Cr_2O_7$, the saturated adsorption capacities are 0.17 g $Cr_2O_7^{2-}$ g^{-1} for TPE-COP and 0.06 g $Cr_2O_7^{2-}$ g^{-1} for PY-COP. These results demonstrate the superior adsorption performance of TPE-COP compared to PY-COP, highlighting the influence of structural design on adsorption efficacy.

1. Introduction

Research into efficient methods for wastewater remediation has become a top priority for the scientific community due to the rapid increase in freshwater demand and the escalating contamination of water resources.[1] Among the various contaminants, toxic oxoanions are particularly prevalent in water and contribute significantly to severe pollution, posing a global threat to ecosystems. This issue has been exacerbated by rapid industrialization and widespread urbanization.[2,3] The United States Environmental Protection Agency has classified several inorganic anions, including $Cr_2O_7^{2-}$, CrO_4^{2-}, MnO^{4-}, ReO^{4-}, and TcO^{4-}, as priority pollutants.[4–6] Wastewater treatment has made use of several advanced methods, such as adsorption,[7] catalysis,[8] membrane filtration,[9] precipitation,[10] condensation,[11] ion exchange,[12] and biodegradation.[13] Among these, adsorption and ion exchange methods are particularly attractive for sewage treatment due to their high efficiency and low processing costs.[14]

Porous materials, including metal–organic frameworks (MOFs) and covalent organic frameworks (COFs), have been widely utilized for the adsorption of various pollutants in aqueous solutions.[6] Porous materials with covalent linkages, such as porous organic polymers (POPs), are often preferred over MOFs due to their superior physical and chemical stability in diverse acidic and basic environments.[15–17] Recently, a new class of porous materials

J.-S. Wong, M. Younis, P.-C. Hu, C.-Y. Hsin, H. Yang, R.-H. Lee
Department of Chemical Engineering
National Chung Hsing University
Taichung 402, Taiwan
E-mail: rhl@dragon.nchu.edu.tw

M. Younis
Chemistry Department
Faculty of Science
New Valley University
El-Kharja 72511, Egypt

P.-H. Chen, P.-L. Liu
Graduate Institute of Precision Engineering
National Chung Hsing University
Taichung 40227, Taiwan
E-mail: pliu@dragon.nchu.edu.tw

The ORCID identification number(s) for the author(s) of this article can be found under https://doi.org/10.1002/adem.202501601.

DOI: 10.1002/adem.202501601

P.-L. Liu
Department of Applied Materials and Optoelectronic Engineering
National Chi Nan University
Nantou 54561, Taiwan

Y.-E. Liang, Y.-T. Chan
Department of Chemistry
National Taiwan University
Taipei 106319, Taiwan

R.-H. Lee
Department of Chemical Engineering and Materials Science
Yuan Ze University
Taoyuan 320, Taiwan

gaining increasing attention for scavenging ionic pollutants is ionic covalent organic polymers (ICOPs). These materials have shown promise for removing iodide/polyiodide species, oxoanions, and others through simple ion exchange processes.[18,19] Due to their strong redox properties and ionic nature, ICOPs, particularly those utilizing viologen as a bridging unit, have become attractive for various applications, including gas storage, memory devices, energy storage, and ion separation.[20]

Das et al. made significant advancements in this area in 2017 by synthesizing a spherical ionic covalent organic polymer (COP) with 1,1′-bis(2,4-dinitrophenyl) dichloride 4,4′-bipyridinium (DNP-BP) as the bridging unit and hexakis(4-aminophenoxy) cyclotriphosphazene (P2) as the core.[21] The profusion of positively charged pyridine structures in this COP enabled rapid replacement of heavy metal anions in solution. Notably, it was able to adsorb all MnO_4^- ions from a 1×10^{-4} M $KMnO_4$ solution within just 1 min. Building on this work, in 2018, the same research group synthesized two COPs with different morphologies: covalent organic tubes (COTs) and covalent organic nanosheets (CONs).[22] These were created by modifying the core structure and were used for the adsorption of iodide ions in solution, leveraging the anion-binding properties of the viologen backbone. Their results showed that COTs, with their higher planarity, allowed iodide ions to enter the COP structure more quickly, leading to faster adsorption compared to CONs. Sarkar et al. synthesized a redox-active, multifunctional ionic porous organic polymer (iPOP-Bpy) with innovative design features, including exchangeable bromide ions and a viologen-based redox-active building block.[23] This advanced material demonstrated exceptional iodine adsorption capabilities across multiple phases, achieving remarkable uptake capacities: 540 wt% in the vapor phase, 1009.77 mg g^{-1} in the organic phase, and an outstanding 3921.47 mg g^{-1} in the aqueous phase. A distinctive feature of this polymer is its exceptionally rapid adsorption kinetics, maintaining high efficiency across all three phases. In 2024, the same research group synthesized three iPOPs using a common viologen-based cationic building block (ZN-NH2). By carefully selecting building blocks with varying sizes and electron densities, the researchers created three distinct polymers—iPOP-ZN1, iPOP-ZN2, and iPOP-ZN3. These polymers demonstrated remarkable versatility in environmental remediation, effectively adsorbing inorganic anions, anionic organic dyes from aqueous solutions, and capturing iodine vapor in solid-state configurations.[1] Additionally, Hassan et al. synthesized an ionic porous organic polymer (iPOP-6) using water as a solvent, which exhibited outstanding performance as an adsorbent for toxic water pollutants. The material demonstrated remarkable ion exchange-based adsorption capabilities for MnO_4^- and I_3^- ions, with distribution coefficients (Kd) exceeding 10^5 mL g^{-1}, indicating superior pollutant removal efficiency. Notably, iPOP-6 was highly effective in scavenging these contaminants from various water samples, showcasing its potential as an energy-efficient and versatile water treatment solution.[19]

Inspired by these previous studies, our research aims to further investigate the effect of morphology on anion exchange in solution by synthesizing ionic COPs with different core structures. Using the Zincke reaction, we will synthesize COPs with 1,1′-bis(2,4-dinitrophenyl) dichloride 4,4′-bipyridinium (BDB), an electron-accepting dicationic organic structure known for its excellent reversible redox properties and fast electron transfer ability,[24] as the bridging unit. We will employ pyrene derivatives and tetraphenylethene as cores, adjusting the planarity of the core to explore the influence of morphology and the abundance of positively charged pyridine structures on the adsorption of ions from ionic solutions.

2. Experimental Section

2.1. Materials and Methods

All reagents were purchased from commercial suppliers and used without further purification. Magnesium sulfate, methanol, and potassium carbonate were purchased from Sigma–Aldrich. Zinc powder, benzophenone, 2,4-dinitrochlorobenzene, and sodium dichromate dihydrate were purchased from Alfa Aesar. Ethyl acetate and acetone were purchased from UR. Acetonitrile, 4,4′-bipyridine, pyrene, 1,1′-bis(diphenylphosphino) ferrocene dichloropalladium(II), and nitrobenzene were purchased from Acros. 1,4-Dioxane, tetrahydrofuran, and potassium permanganate were purchased from J. T. Baker. Sodium hydroxide and nitric acid were purchased from Honeywell. *n*-Hexane and ethanol were purchased from ECHO. Dichloromethane was purchased from Duksan. Titanium tetrachloride was purchased from Showa. Glacial acetic acid was purchased from Scharlau. Hydrochloric acid was purchased from Aencore. Tin(II) chloride dihydrate was purchased from Mallinckrodt. Sodium bicarbonate was purchased from Riedel-de Haën. Bromide was purchased from KANTO Chemical. 4-(4,4,5,5-Tetramethyl-1,3,2-dioxaborolan-2-yl)aniline was purchased from Matrix. The detailed synthesis routes of DBD, $TPE(NH_2)_4$, and $PY(NH_2)_4$ are illustrated in Scheme S1–S3, Supporting Information. BDB was synthesized according to previous article,[21] briefly 4,4′-bipyridine refluxed with 2,4-dinitrochlorobenzene at 95 °C and maintained for 3 days, also 1,1,2,2-tetrakis(4-aminophenyl)ethene ($TPE(NH_2)_4$),[25] Tin(II) chloride dihydrate with 1,1,2,2-tetrakis(4-nitrophenyl)ethene refluxed in ethanol for 12 h, and 1,3,6,8-tetrakis(4-aminophenyl) pyrene ($PY(NH_2)_4$),[25] 1,3,6,8-Tetrabromopyrene and 4-(4,4,5,5-tetramethyl-1,3,2-dioxaborolan-2-yl)aniline refluxed at 115 °C for 3 days in presence of $Pd(PPh_3)_4$. The chemical structures of the synthesized organic compounds (DBD, $TPE(NH_2)_4$, and $PY(NH_2)_4$) were characterized using Fourier transform infrared (FTIR) and ^1H NMR spectroscopy, as shown in Figure S1–S7, Supporting Information.

2.2. Synthesis of ICOPs

As shown in **Scheme 1**, the TPE-COP was synthesized via a condensation reaction in a Pyrex tube. A reaction mixture containing $TPE(NH_2)_4$ (0.035 g, 0.089 mmol) and BDB (0.15 g, 0.27 mmol) was prepared in a solvent system consisting of 1,4-dioxane (2 mL), *N,N*-dimethylacetamide (DMAc) (0.2 mL), and acetic acid solution (6 M, 0.2 mL). The heterogeneous mixture was subjected to ultrasonication for 15 min to achieve uniform dispersion. The reaction mixture then underwent multiple freeze–pump–thaw cycles to remove dissolved gases. Subsequently, the reaction mixture was heated to 100 °C and maintained at this

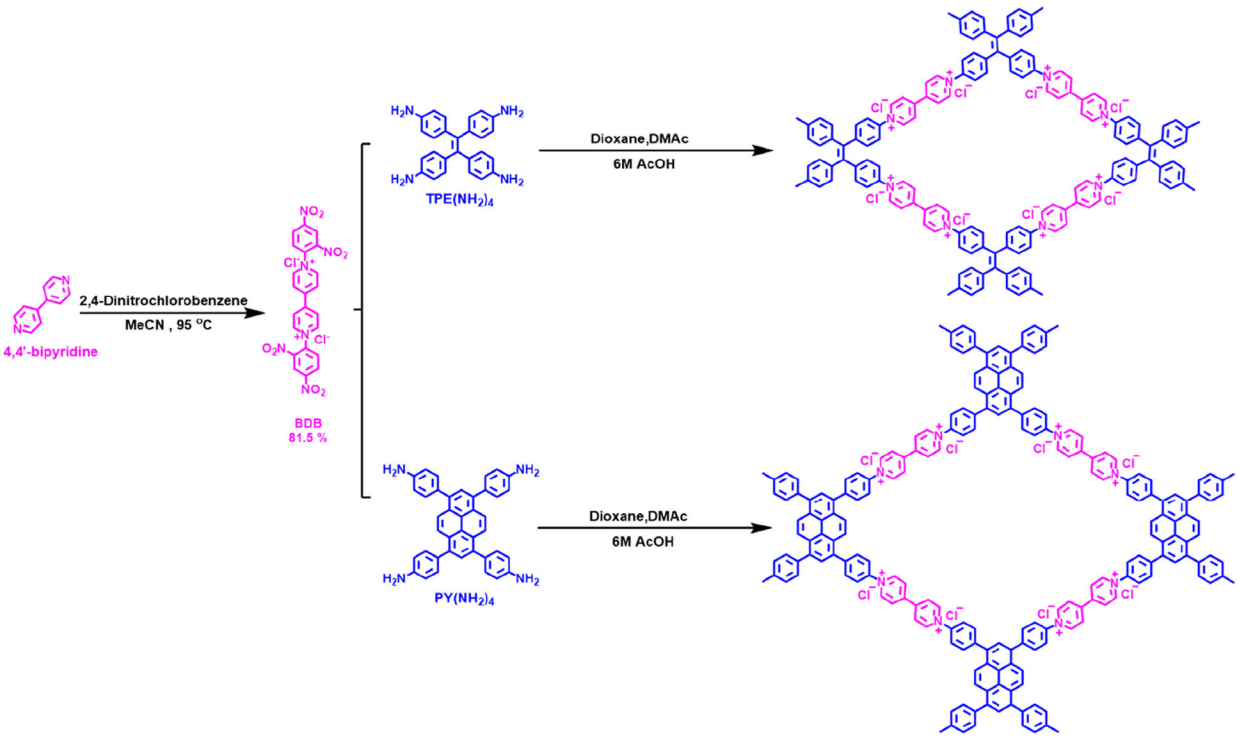

Scheme 1. Synthesis of TPE-COP and PY-COP.

temperature for seven days. Upon completion, the reaction was cooled to room temperature. The resulting product was washed with methanol and acetone, and the solid was collected by vacuum filtration. Further purification was achieved by Soxhlet extraction, first with methanol for 24 h, followed by acetone for an additional 24 h. The final product was dried in a vacuum oven at 100 °C, yielding TPE-COP (0.047 g).

As shown in Scheme 1, the **PY-COP** was synthesized following a similar procedure to that of TPE-COP, with modifications to the starting materials. In a Pyrex tube, $(PY(NH_2)_4)$ (0.05 g, 0.089 mmol) was reacted with BDB (0.15 g, 0.27 mmol) in a solvent mixture of 1,4-dioxane (2 mL), *N,N*-dimethylacetamide (DMAc) (0.2 mL), and acetic acid solution (6 M, 0.2 mL). The reaction mixture was sonicated for 15 min to ensure homogeneous dispersion. Following sonication, the solution was subjected to multiple freeze–pump–thaw cycles for degassing. The reaction mixture was heated to 100 °C and maintained at this temperature for seven days. After completion, the reaction was cooled to room temperature. The product was washed with methanol and acetone, and the solid was collected by vacuum filtration. Further purification was carried out using Soxhlet extraction, first with methanol for 24 h, followed by acetone for an additional 24 h. The final product was dried in a vacuum oven at 100 °C, yielding PY-COP (0.081 g).

2.3. Characterization

The HORIBA FT-720 FTIR spectrometer was used to record FTIR spectra. ^{1}H NMR spectra were obtained with a Varian Unity Inova-600 600 MHz high field NMR spectrometer. ^{13}C NMR spectra were obtained with a Bruker Avance III 400 NMR spectrometer. The morphologies of the ICOPs were examined using field emission scanning electron microscopy (FE-SEM, JSM 7401F; JEOL, Japan) and high-resolution transmission electron microscopy (TEM, JEOL JEM-1400). Thermal stability of ICOPs were investigated with a PerkinElmer TGA-7 thermogravimetric analyzer (heating rate of 10 °C min^{-1}). The anionic adsorption performance of the ICOPs was monitored by UV–vis spectra measurements on a Hewlett-Packard 8453 UV–vis spectrophotometer. The specific surface area and pore size distributions of samples were determined by the Brunauer–Emmett–Teller (BET) method and Barret–Joyner–Halenda theory, respectively. The chemical compositions of the ICOPs were analyzed using X-ray photoelectron spectroscopy (XPS) with a ULVAC-PHI PHI500 VersaProbe instrument.

2.4. Adsorption Experiments

For the adsorption, we directly used the resultant ICOP as adsorbents for anion in aqueous solution. Generally, COP (2 mg for $Na_2Cr_2O_7$, 1 mg for $KMnO_4$) was added to $Na_2Cr_2O_7$ solutions (4 mL) or $KMnO_4$ solutions (4 or 8 mL) at different concentrations (1×10^{-3} M, 1×10^{-4} M). The mixtures were placed in an ultrasonic bath for constant agitation to assist in dispersion. After sonication, the absorption values were detected using a UV–vis spectrophotometer, and these values were substituted into the calibration curve formulas (Figure S8 and Figure S9, Supporting Information) to obtain the postadsorption concentration. The adsorption efficiency formula was then used to determine the concentration of oxygen-containing metal anions absorbed by the COP.

$$\text{Adsorption efficiency}\,(\%) = \frac{(C_0 - C)}{C_0} * 100 \quad (1)$$

where C_0 is the initial concentration and C is the solution concentration after a specific time of COP addition.

3. Results and Discussion

3.1. Characterization of TPE-COP and PY-COP

Synthetic strategies for ICOPs are illustrated in Scheme 1. Typically, ICOPs were synthesized via a Zincke reaction using $TPE(NH_2)_4$ and $PY(NH_2)_4$ as core building blocks, which were reacted with the Zincke salt BDB in 6 M acetic acid. The acidic medium is essential for the reaction,[26] as it promotes the formation of the azatriene intermediate and facilitates subsequent cyclization, resulting in high yields. Notably, the synthesis of PY-COP in acetic acid afforded a higher yield compared to reactions performed in the absence of acetic acid.[22] To confirm the structure of TPE-COP and Py-COP, FTIR spectroscopy was performed. As shown in **Figure 1**, for TPE-COP, the primary absorptions include C═C─H stretching on the benzene ring at 3110 and 3031 cm^{-1}, as well as C═N stretching at 1635 cm^{-1}, and C═C stretching of the benzene ring at 1504 cm^{-1}. Notably, the absence of NO_2 asymmetric and symmetric stretching (1536 and 1346 cm^{-1}) from the BDB monomer and NH_2 bending (1617 cm^{-1}) from $TPE(NH_2)_4$ confirms the successful formation of the poly(pyridinium) salt product. Also, for PY-COP, the primary functional group absorptions include C═C─H stretching on the benzene ring at 3116 and 3020 cm^{-1}, C═N stretching at 1635 cm^{-1}, and C═C stretching of the benzene ring at 1504 cm^{-1}. Notably, the absence of NO_2 asymmetric and symmetric stretching (1536 and 1346 cm^{-1}) from the BDB monomer, as well as the NH_2 bending (1612 cm^{-1}) from $PY(NH_2)_4$, confirms the successful formation of the poly(pyridinium) salt product.

To further characterize the structures of the products, solid-state ^{13}C NMR spectra were also used to confirm the presence of specific functionalities at the molecular level. For TPE-COP, the signals between 105 and 137 ppm (a–d,g) correspond to the ^{13}C signals of the conjugated C═C structure in the core $TPE(NH_2)_4$ and the C═C structure on the pyridine ring of BDB. The signals between 137 and 154 ppm (e,f, and h) represent the ^{13}C signals of the C─N^+ bonds between $TPE(NH_2)_4$ and BDB, as well as the C═N and C═C bonds on the pyridine ring (**Figure 2**a). For PY-COP, the signals between 110 and 139 ppm (b,e,f,g,h,j,k,i, and l) correspond to the ^{13}C signals of the conjugated C═C structure in the core $PY(NH_2)_4$ and the BDB branches. The signals between 140 and 165 ppm

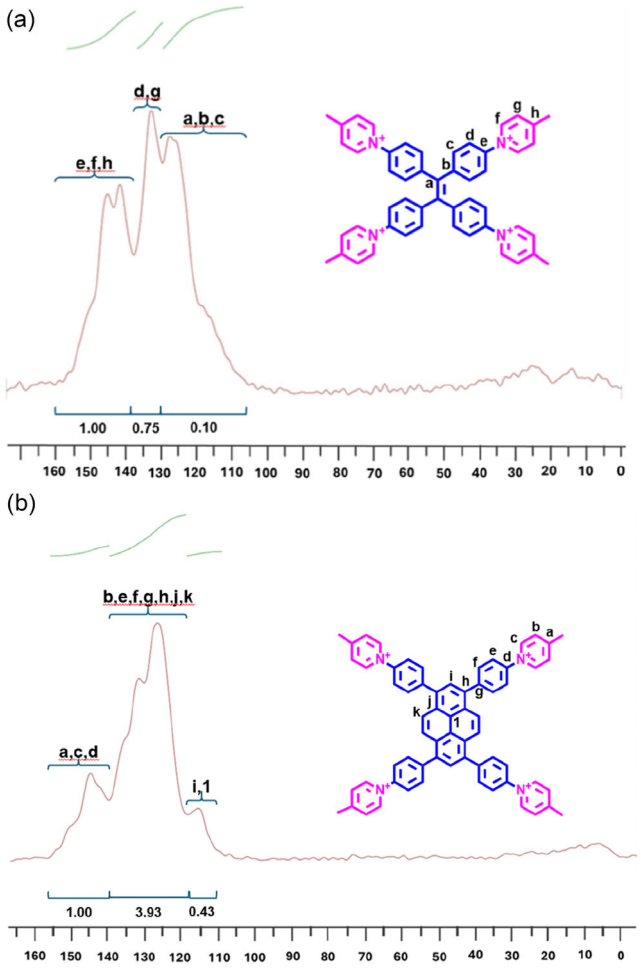

Figure 2. ^{13}C NMR SPECTRA a) TPE-COP and b) PY-COP.

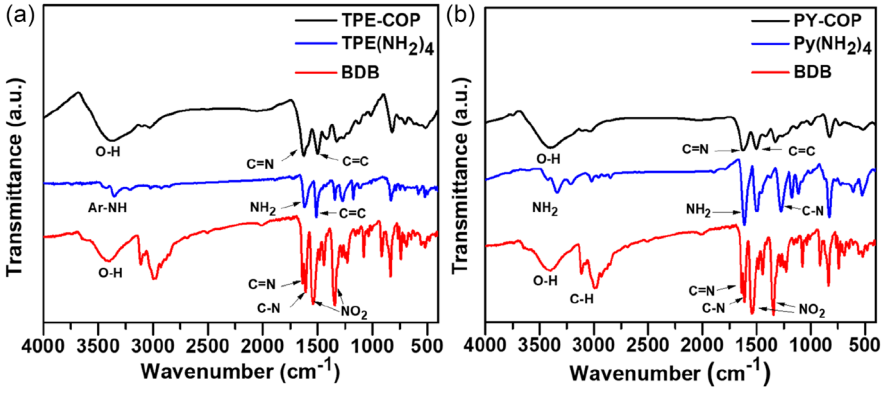

Figure 1. FTIR spectra of a) TPE-COP and b) PY-COP.

(a,c, and d) represent the ^{13}C signals of carbon atoms influenced by the nitrogen ions of the pyridine ring in BDB (Figure 2b).

To further investigate the structure of the ICOPs, X-ray diffractometer (XRD) was employed. TPE-COP and PY-COP show a broad diffraction peak centered at $2\theta = 22.5°$, indicating an amorphous or low-crystalline nature (**Figure 3**). SEM and TEM images further provide deep insight into the microstructure of the ICOP. As shown in **Figure 4**a, the FE-SEM image of TPE-COP reveals a diverse array of spherical aggregates with a broad size distribution. The TEM image in Figure 4c shows that these spherical particles have a solid interior. The aggregation of spherical particles is consistent with Zhang et al.'s findings,[27] suggesting that a core without hydrogen bonding favors the formation of spherical particles with different particle sizes. The FE-SEM image of PY-COP reveals aggregated and stacked irregular structures. Figure 4b offers a clearer view of this morphology, while the TEM image in Figure 4d further confirms that PY-COP consists of multiple stacked layers of irregular structures.

Furthermore, the thermal stability of the ICOPs was investigated by thermogravimetric analysis. **Figure 5**a shows the thermogravimetric analysis (TGA) curves of TPE-COP, TPE$(NH_2)_4$, and BDB. Under nitrogen at 20 °C per min, TPE$(NH_2)_4$ decomposes at 360.8 °C with a char residue of 34.6%, while BDB has a lower decomposition temperature of 179.3 °C and minimal residue. TPE-COP, synthesized using BDB, has a lower decomposition temperature of 264.6 °C but a higher char residue (47.1%) due to polymerization. Figure 5b presents PY-COP, PY$(NH_2)_4$, and BDB. PY$(NH_2)_4$ decomposes at 517.0 °C with 38.9% residue, attributed to its stable polycyclic structure. Consequently, PY-COP shows greater thermal stability than TPE-COP, with a decomposition temperature of 320.4 °C and a char residue of 65.9%.

Nitrogen adsorption isotherms revealed that both TPE-COP and PY-COP exhibited BET surface areas of 15.6 and 15.3 $m^2 g^{-1}$, respectively (**Figure 6**a,b). Both materials displayed Type-II adsorption isotherms, indicative of non or low macroporous structures. The relatively low surface areas may be attributed to the pores being

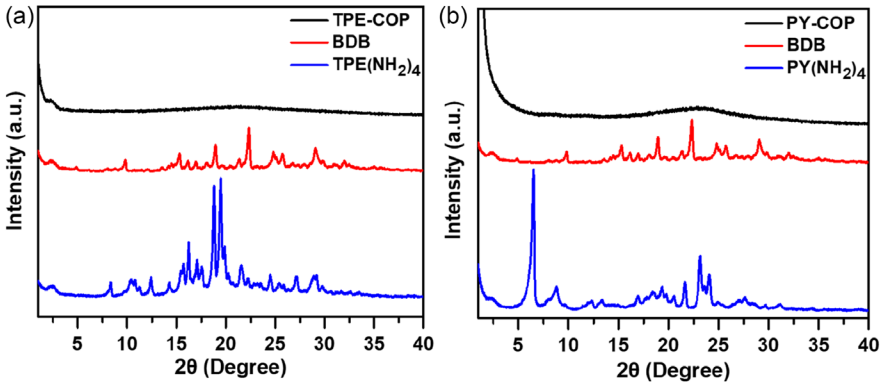

Figure 3. XRD patterns of a) TPE-COP and b) PY-COP.

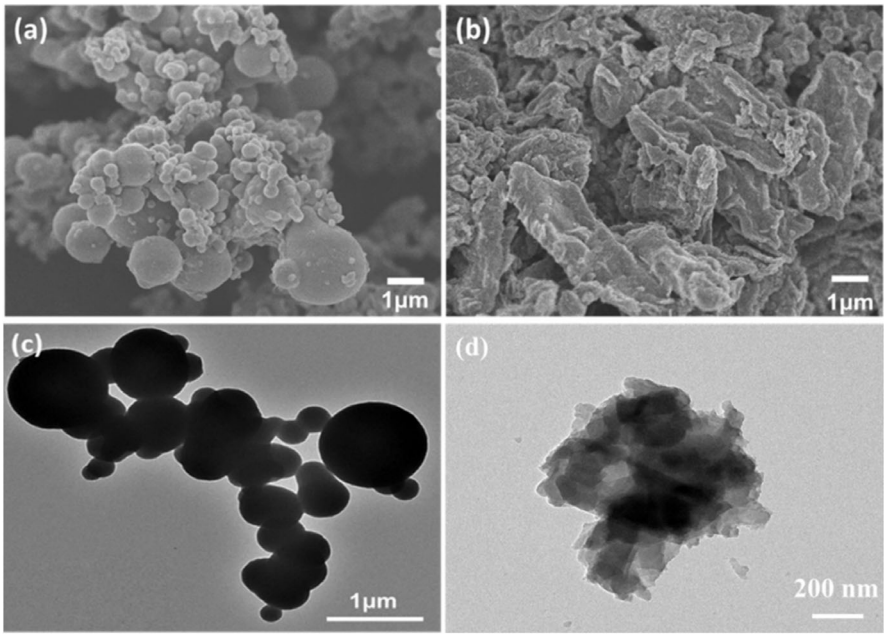

Figure 4. a,b) SEM and c,d) TEM images of TPE-COP and PY-COP [(a,c) TPE-COP and (b,d) PY-COP].

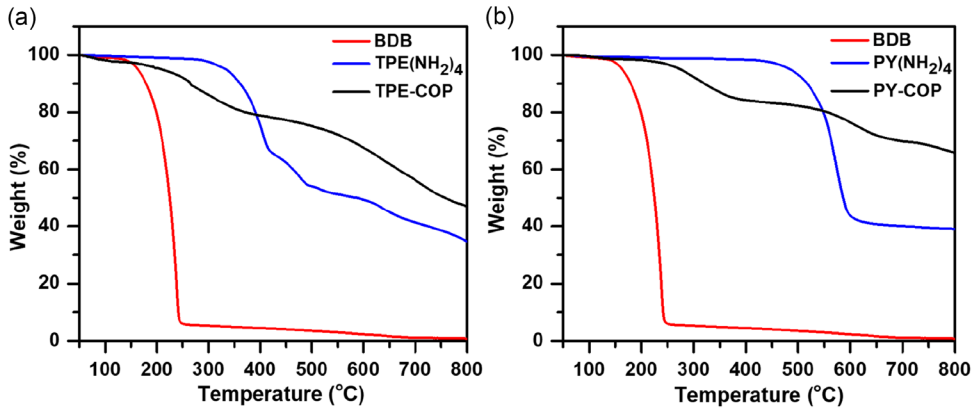

Figure 5. TGA curves of a) TPE-COP and b) PY-COP.

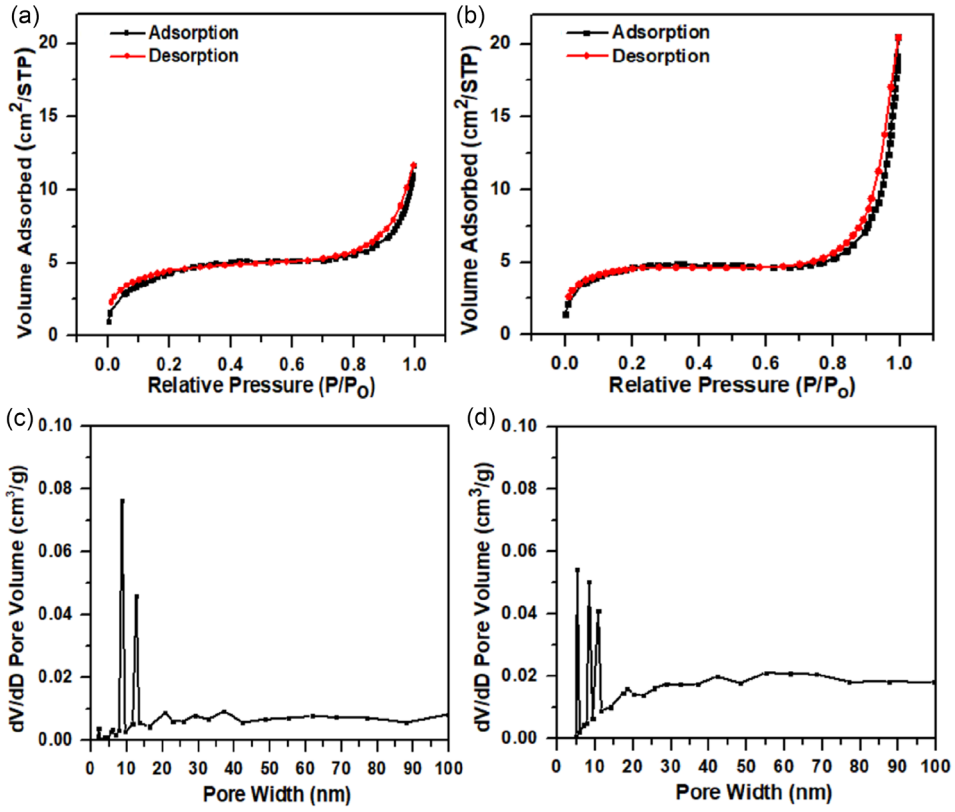

Figure 6. Isothermal nitrogen adsorption-desorption curves and pore size distribution curves of a,c) TPE-COP and b,d) PY-COP.

filled by chloride ions, preventing accurate detection of microporosity.[22] Pore size distributions were calculated using BET analysis, but no distinct micropore distribution was observed due to blocked pores. Nonetheless, mesopore size distributions for TPE-COP ranged from 8 to 13 nm (8.56 and 12.62 nm), while those for PY-COP ranged from 5 to 21 nm (5.19, 8.40, and 21 nm) (Figure 6c,d).

XPS analysis of TPE-COP and PY-COP (**Figure 7**, **8**) elucidates their chemical bonding and electronic structure. Both materials exhibit similar spectral characteristics with slight variations in binding energies. C 1*s* spectrum of TPE-COP (Figure 7b) reveals peaks at 283.49 eV (C═C bonds) and 284.68 eV (C—N bonds), while its N 1*s* spectrum (Figure 7c) shows peaks at 398.40 eV (N^{+}. bonding) and 401.02 eV (N^{++} bonding). Similarly, C1s of PY-COP spectrum (Figure 8b) displays peaks at 283.80 eV (C═C bonds) and 285.22 eV (C—N bonds), with N 1*s* peaks (Figure 8c) at 398.82 eV (N^{+}. bonding) and 401.00 eV (N^{++} bonding). Cl 2*p* spectra for both materials (Figure 7d and 8d) indicate Cl^{-} ions. The observed $N^{+\cdot}$ bonding is attributed to XPS excitation or the donor–acceptor (D–A) effect, as supported by Cao et al.[28] and Hua et al.[29] The XPS result confirms that the viologen moiety's redox-active behaviors are underscored by the presence of a substantial peak at 398.40 and 401.02 eV in samples, which is attributed to the reduced radical cationic nitrogen

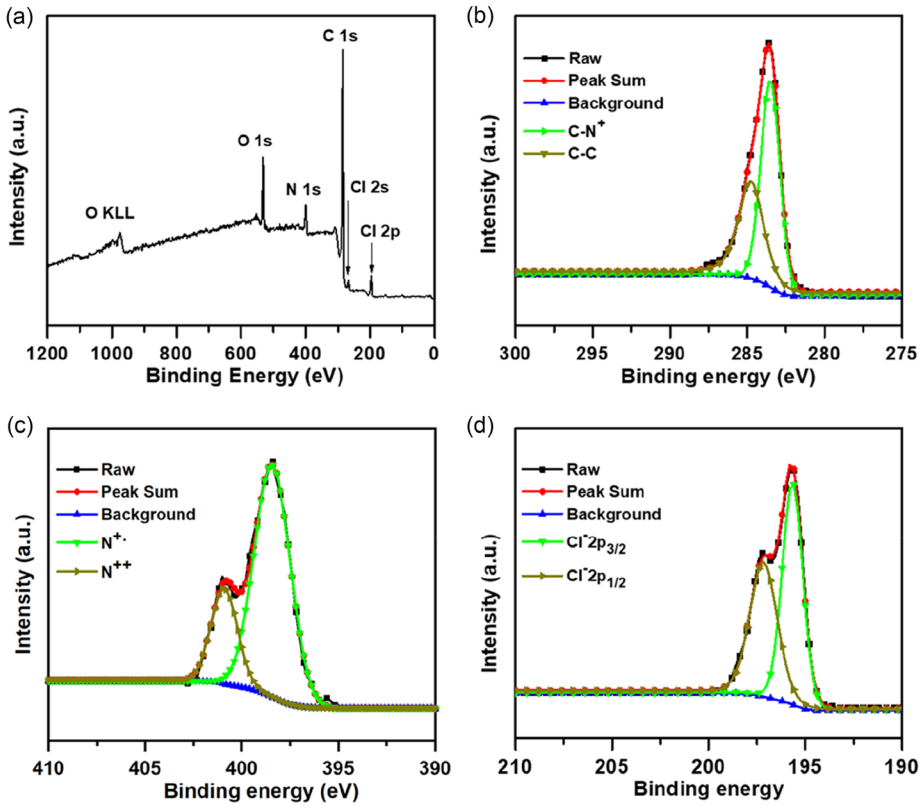

Figure 7. a) XPS survey spectrum of TPE-COP. XPS spectra b) C 1s, c) N 1s, and d) Cl 2*p* binding energies of TPE-COP.

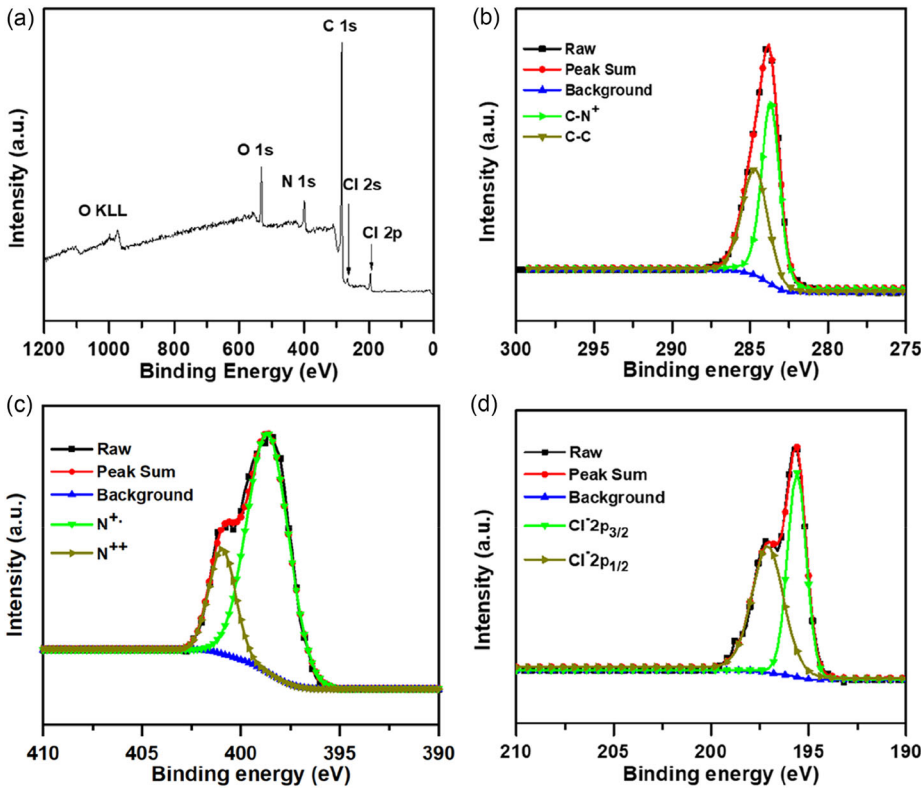

Figure 8. a) XPS survey spectrum of PY-COP. XPS spectra b) C 1s, c) N 1s, and d) Cl 2*p* binding energies of PY-COP.

species (N^{+}.) and the dicationic (N^{++}) of the viologen unit.[20,30] The results indicated that the absorption peak corresponding to the reduced radical cationic nitrogen species was much stronger than that of the dicationic species in the viologen units for both TPE-COP and PY-COP (Figure 7c and 8c). This suggests that a higher proportion of the reduced radical cationic nitrogen species was present in the samples. Oxygen signals in full spectra (Figure 7a and 8a) are due to water vapor captured by nitrogen ions via hydrogen bonding, providing comprehensive insights into the materials' chemical structures and electronic properties.

3.2. Adsorption Studies

The UV–vis absorption spectra of TPE-COP and PY-COP in potassium permanganate ($KMnO_4$) solutions at different concentrations and time intervals. In the 1×10^{-4} M $KMnO_4$ solution (**Figure 9**a,b), both TPE-COP and PY-COP successfully removed the MnO_4^- ions after agitation, indicating that the 1×10^{-4} M concentration was too dilute to fully assess their permanganate removal capacities. As a result, the concentration was increased tenfold to 1×10^{-3} M to better evaluate the maximum removal capacities of TPE-COP and PY-COP within 1 h.

In the 1×10^{-3} M $KMnO_4$ solution (Figure 9c,d), TPE-COP removed over half (57%) of the MnO_4^- ions within the first 15 min, based on the absorbance at 525 nm (with an initial value of 2.776). In comparison, PY-COP removed 32% of the MnO_4^- ions during the same time. However, PY-COP exhibited a notable decrease in ion removal rate after 30 min. This slowdown in PY-COP is likely due to its sheet-like structure, which allows the solution to penetrate the material more quickly,

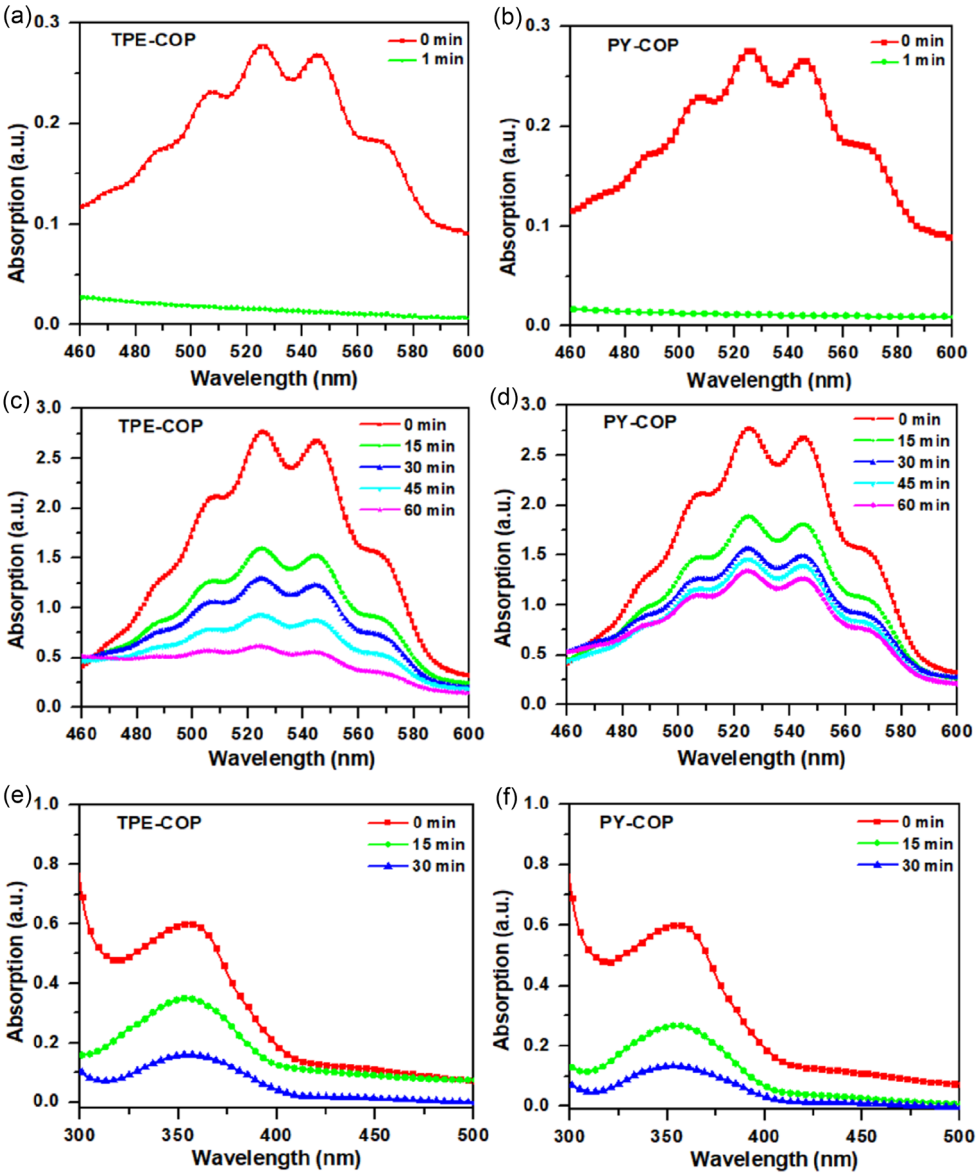

Figure 9. UV–vis spectra of TPE-COP and PY-COP in a,b) 1×10^{-4} M $KMnO_4$ solution, c,d) 1×10^{-3} M $KMnO_4$ solution, and e,f) 1×10^{-4} M $Na_2Cr_2O_7$ solution at different time intervals.

enabling a faster initial ion exchange but resulting in earlier saturation. After 1 h, TPE-COP had removed 78% of the MnO_4^- ions, while PY-COP removed only 52%. Although PY-COP possesses a larger specific surface area, TPE-COP's superior ion removal capacity can be attributed to its smaller core size and the higher concentration of N^+ ions per unit mass. These factors suggest that the number of active sites (N^+ ions) has a more significant impact on ion exchange efficiency than surface area, explaining why TPE-COP exhibits a higher overall removal efficiency compared to PY-COP.

The UV–vis absorption spectra of TPE-COP and PY-COP in 1×10^{-4} M $Na_2Cr_2O_7$ solution were measured over time, with the absorption range of $Na_2Cr_2O_7$ spanning from 230 to 700 nm Figure 9e,f. Both TPE-COP and PY-COP exhibited slower ion exchange rates for $Cr_2O_7^{2-}$ ions compared to MnO_4^- ions at the same concentration. After 15 min, it was observed that the ion exchange rate for PY-COP decreased more rapidly, likely due to its sheet-like structure, which facilitates easier penetration of the ion-containing solution and leads to a faster initial exchange followed by quicker saturation. At the 30 min interval, TPE-COP and PY-COP had removed 74% and 78% of the $Cr_2O_7^{2-}$ ions from the solution, respectively, based on an initial absorbance of 0.6 at 356 nm for the 1×10^{-4} M $Na_2Cr_2O_7$ solution (denoted as C_0). The slower exchange rates for $Cr_2O_7^{2-}$ ions compared to MnO_4^- ions can be attributed to the inverse correlation between ion size and exchange rate.[28] Because $Cr_2O_7^{2-}$ ions are larger than MnO_4^- ions, their exchange occurs at a slower rate.

Table 1 presents a comprehensive comparison of adsorption performance for $Cr_2O_7^{2-}$ and MnO_4^- oxyanions across various ICOPs and related materials reported in the literature. The comparative analysis reveals significant variations in removal efficiency and selectivity patterns among different structural frameworks. ImCON1 exhibits the highest overall performance in this comparative study, demonstrating exceptional dual functionality with $Cr_2O_7^{2-}$ adsorption capacity of 1118 mg g^{-1} and substantial MnO_4^- uptake of 694.5 mg g^{-1}. These values represent the current benchmark performance for simultaneous oxyanion removal from aqueous solutions. However, the viologen-based COPs investigated in this study demonstrate distinctive and competitive performance characteristics that merit detailed examination. TPE-COP achieves remarkable selectivity toward permanganate ions, exhibiting the highest MnO_4^- adsorption capacity of 770 mg g^{-1} among all materials evaluated. This exceptional performance surpasses even the benchmark ImCON1 material for permanganate removal while maintaining moderate $Cr_2O_7^{2-}$ adsorption capacity of 170 mg g^{-1}. In contrast, PY-COP demonstrates more balanced dual functionality, achieving moderate adsorption capacities of 60 mg g^{-1} for $Cr_2O_7^{2-}$ and 350 mg g^{-1} for MnO_4^-. The contrasting performance profiles between TPE-COP and PY-COP highlight the critical influence of structural design parameters on adsorption behavior and selectivity. While TPE-COP excels in permanganate removal applications, PY-COP offers more balanced dual-oxyanion functionality. Both viologen-containing frameworks demonstrate competitive performance within the current literature, with TPE-COP establishing new performance benchmarks for MnO_4^- removal specifically. These findings position viologen-based COPs as innovative and highly competitive materials for environmental remediation applications. The structure–property relationships revealed through this comparative analysis provide valuable insights into the rational design of selective adsorbents targeting specific oxyanion contaminants in water treatment technologies.

Table 1. Comprehensive comparison of adsorption performance.

ICOPs	Capacities (MnO_4^-) [mg g^{-1}]	Capacities ($Cr_2O_7^{-2}$) [mg g^{-1}]	Ref.
TPE-COP	770	170	This work
PY-COP	350	60	This work
ICOF-2	334	253	[5]
HB-IPOP	–	292	[29]
TBPM	–	411.12	[36]
ImCON1	694.5	1118	[37]
Tp-DG_{Cl}	–	360.02	[38]
BPTP COF	448.09	–	[39]

3.3. Adsorption Mechanism

To distinguish between adsorption and absorption phenomena, TGA of both COPs following MnO_4^- uptake revealed negligible differences in ash content compared to pristine samples (Figure S10, Supporting Information), confirming that the removal mechanism proceeds via surface adsorption rather than bulk diffusion into the polymer matrix. **Figure 10** illustrates the dual adsorption pathways operative in viologen-based COPs for oxyanion removal, where the viologen COP architecture incorporates bipyridinium units as primary adsorption sites characterized by inherent positive charges initially balanced by chloride counter-ions within an extended aromatic polymer framework. The material functions through two complementary mechanisms: ion exchange, where loosely bound chloride ions are selectively displaced by oxyanions based on the polymer's preferential affinity for target species following stoichiometric replacement principles, and electrostatic attraction, enabling

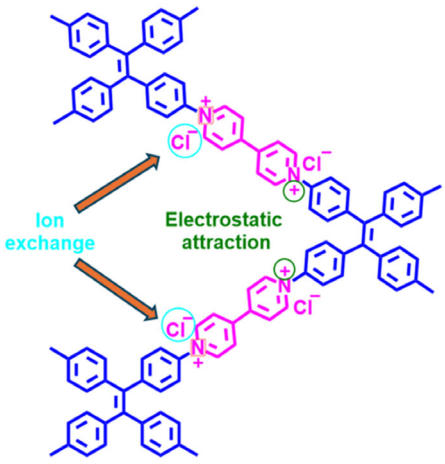

Figure 10. ICOP adsorption mechanism.

direct Coulombic interactions between positively charged viologen sites and negatively charged oxyanion species. This dual-mode mechanism proves particularly effective because viologen units provide both strong electrostatic binding sites and potential redox interaction capabilities with target ions, while the robust COP framework maintains structural integrity and facilitates efficient mass transfer processes. XPS analysis of ICOPs following MnO_4^- and $Cr_2O_7^{2-}$ adsorption (Figure S11, Supporting Information) provides experimental validation of this proposed mechanism, with spectra clearly revealing the presence of Mn, Cr, and Cl peaks, confirming that positively charged nitrogen centers (N^+) serve as electrostatic interaction sites for oxyanion adsorption. Energy-dispersive X-ray analysis (Figure S12-S15, Supporting Information) of COPs after adsorption further confirms this mechanism, specifically showing that TPE-COP exhibits significantly higher Mn content compared to PY-COP following MnO_4^- exposure, while chloride ratios remain relatively unchanged, indicating that the primary mechanism involves electrostatic adsorption rather than complete ion exchange. The observed reduction in chloride ion peak intensity simultaneously corroborates the occurrence of partial ion exchange processes during adsorption, and these complementary analytical findings support the dual-mechanism model, demonstrating the effectiveness of viologen-based COPs for selective oxyanion remediation through both ion exchange and electrostatic interactions.

3.4. First-Principles Insights into Adsorption and Stacking Behavior

To complement the experimental findings and provide microscopic insights into the adsorption mechanism, we performed density functional theory (DFT) calculations. The molecular-level analysis serves three purposes: 1) to obtain optimized geometries of TPE- and PY-based frameworks and their anion complexes, thereby revealing local structural characteristics; 2) to evaluate adsorption energies of Cl^-, MnO_4^-, and $Cr_2O_7^{2-}$, allowing a quantitative comparison of intrinsic binding strengths; and 3) to examine the stacking behavior under different interlayer distances, clarifying the role of oxoanions in promoting aggregation. Our DFT calculations were performed using the Vienna Ab initio Simulation Package.[31–33] The generalized gradient approximation with the Perdew–Wang 91 functional was employed,[34,35] together with a plane-wave cutoff energy of 450 eV and Monkhorst–Pack *k*-point meshes of $3 \times 3 \times 1$ (TPE) and $2 \times 2 \times 1$ (PY). A vacuum spacing of 40 Å was set along the *c*-axis to minimize image interactions. Model compositions were $C_{46}H_{32}N_4$ (TPE) and $C_{60}H_{38}N_4$ (PY), both containing four quaternized nitrogen atoms.

The optimized structures of the pristine frameworks and their lowest energy adsorption complexes with Cl^-, MnO_4^-, and $Cr_2O_7^{2-}$ are shown in **Figure 11**, while the corresponding adsorption energies (ΔE_{ads}) are summarized in **Table 2**. The adsorption energy was calculated according to

$$\Delta E_{ads}(eV) = E_{COP+anion} - E_{COP} - E_{anion} \quad (2)$$

where adsorption energy, ΔE_{ads}, denotes the binding strength between the COP and the anion. $E_{COP+anion}$ means the total energy of the COP framework with the adsorbed anion. E_{COP} and E_{anion} are the total energy of the isolated COP framework and the isolated anion, respectively. A more negative ΔE_{ads} corresponds to stronger binding between the COP and the anion. The optimized structures of the representative models are displayed in Figure 11. Their corresponding coordinate files are

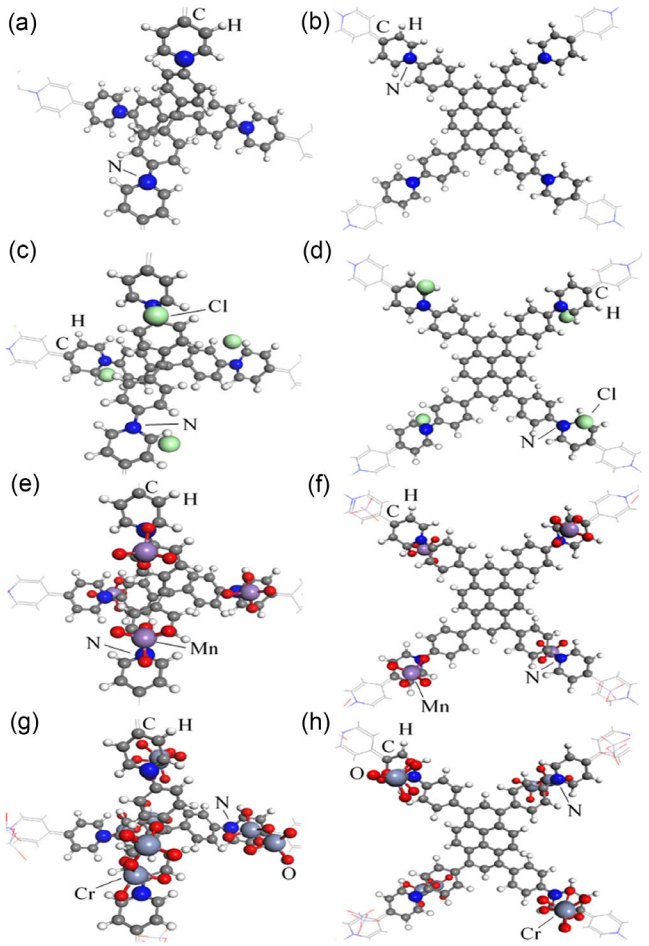

Figure 11. Optimized structures of a) TPE-COP, b) PY-COP, c) TPE-COP with Cl^-, d) PY-COP with Cl^-, e) TPE-COP with MnO_4^-, f) PY-COP with MnO_4^-, g) TPE-COP with $Cr_2O_7^{2-}$, and h) PY-COP with $Cr_2O_7^{2-}$. Color code: C (gray), H (white), N (blue), Cl (green), Mn (purple), Cr (grayish blue), and O (red).

Table 2. Calculated adsorption energies (ΔE_{ads}) and stacking energetics (ΔE_{stack}) of TPE-COP and PY-COP with different anions obtained from first-principles DFT calculations.

Model	ΔE_{ads}	E_{40}	E_{30}	E_{20}	$\Delta E_{stack,30\text{-}40}$	$\Delta E_{stack,20\text{-}40}$
TPE_Cl	−9.351	−569.655	−570.408	−569.574	−0.753	0.081
TPE_MnO_4	−3.123	−690.589	−691.403	−691.323	−0.813	−0.733
TPE_Cr_2O_7	−12.546	−824.306	−828.040	−827.604	−3.734	−3.298
PY_Cl	−8.969	−720.481	−719.307	−719.369	1.174	1.112
PY_MnO_4	−8.884	−847.558	−847.771	−847.276	−0.213	0.282
PY_Cr_2O_7	−10.256	−973.223	−973.696	−973.479	−0.473	−0.256

provided in the Supporting Information, and an online interactive platform (http://140.120.185.45:8501) is available for 3D visualization.

Results in Figure 11 and Table 2 reveal that TPE-COP exhibits markedly stronger stabilization toward oxoanions, especially $Cr_2O_7^{2-}$ ($\Delta E_{ads} = -12.546$ eV), compared with PY-COP ($\Delta E_{ads} = -10.256$ eV), consistent with the higher saturated uptake of $Cr_2O_7^{2-}$ observed experimentally (0.17 g g^{-1} for TPE-COP vs 0.06 g g^{-1} for PY-COP). Although MnO_4^- binding is locally more favorable on the PY model ($\Delta E_{ads} = -8.884$ eV) than on TPE ($\Delta E_{ads} = -3.123$ eV), the experimental results consistently show higher overall uptake for TPE-COP. This apparent discrepancy can be rationalized by considering the N^+ site density per unit mass. Each repeat unit of TPE ($C_{46}H_{32}N_4$, 640.8 g mol^{-1}, 6.24 mmol N^+ g^{-1}) and PY ($C_{60}H_{38}N_4$, 815.0 g mol^{-1}, 4.91 mmol N^+ g^{-1}) contains four quaternized nitrogen atoms, with the lighter TPE core yielding a higher N^+ site density per mass. In other words, TPE-COP provides ≈1.27 times more exchangeable cationic sites per gram than PY-COP. As a result, despite the stronger single-site binding observed for PY, the larger number of accessible sites and the more favorable morphology of TPE-COP lead to superior macroscopic adsorption. These findings highlight the consistency between molecular-scale computational results and bulk-scale experimental measurements.

We mapped the stacking energetics by varying the *c*-axis (interlayer distance) from 40 to 30 and 20 Å (Table 1). For TPE, oxoanions markedly stabilize interlayer approach: $Cr_2O_7^{2-}$ yields a large energy drop ($\Delta E_{stack,\,30-40} = -3.734$ eV; $\Delta E_{stack,\,20-40} = -3.298$ eV), and MnO_4^- also shows an apparent stabilization (−0.813/−0.733 eV), indicating a pronounced stacking propensity with a preferred spacing near ≈30 Å. In contrast, Cl^- gives only a shallow minimum at 30 Å and becomes repulsive at 20 Å. For PY, Cl^- disfavors stacking (positive $\Delta E_{stack,\,30-40}$ and $\Delta E_{stack,\,20-40}$at 30/20 Å), MnO_4^- exhibits only a very shallow minimum around 30–40 Å and becomes unstable at 20 Å, while $Cr_2O_7^{2-}$ shows a slight but consistent stabilization (−0.473/−0.256 eV). These trends are consistent with experiments: oxoanions, particularly $Cr_2O_7^{2-}$, promote closer aggregation in TPE-COP, rationalizing its higher macroscopic uptake, whereas PY-COP exhibits weaker stabilization upon close approach, consistent with irregular morphology but less densely stacked domains. Overall, the DFT simulation results (Table 2) are in good agreement with the experimental adsorption data (Table 1). The calculations indicate that TPE-COP exhibits stronger binding tendencies toward both $Cr_2O_7^{2-}$ and MnO_4^-, consistent with its higher removal capacities observed experimentally; in particular, the outstanding performance of TPE-COP for MnO_4^- uptake is well supported by the favorable structural features revealed by DFT. In contrast, PY-COP demonstrates more balanced but moderate dual functionality in both theory and experiment. These findings confirm that the molecular-scale driving forces identified by theoretical calculations effectively rationalize the macroscopic adsorption behaviors. The consistency between theoretical (DFT) calculations and experimental adsorption measurements highlights the complementarity of the two approaches. Table 2 calculates adsorption energies (ΔE_{ads}) and stacking energetics (ΔE_{stack}) of TPE-COP and PY-COP with different anions obtained from first-principles DFT calculations. Adsorption energies (ΔE_{ads}, eV) were computed as $E_{COP+anion} - E_{COP} - E_{anion}$, with more negative values indicating stronger binding at a single N^+ site. Stacking energetics were evaluated by shortening the *c*-axis from 40 Å (reference) to 30 and 20 Å, where $\Delta E_{stack,\,30-40} = E_{30} - E_{40}$ and $\Delta E_{stack,\,20-40} = E_{20} - E_{40}$. Negative values denote stabilization upon interlayer approach, whereas positive values indicate destabilization. Results reveal pronounced stabilization for oxoanions, particularly $Cr_2O_7^{2-}$ in TPE-COP, while PY-COP generally shows weaker or no stacking tendency.

4. Conclusion

This study successfully synthesized two ICOPs, TPE-COP and PY-COP, via the Zincke reaction. Core structure significantly influenced polymer morphology, resulting in spherical structure for TPE-COP and stacked morphology for PY-COP. Both demonstrated good thermal stability. Anion adsorption studies using $KMnO_4$ and $Na_2Cr_2O_7$ solutions revealed superior performance of TPE-COP, attributed to its higher N^+/C ratio and spherical structure facilitating faster ion removal. Stacked structure of PY-COP resulted in slower adsorption kinetics. These findings highlight the critical role of COP morphology in anion adsorption performance. Future research should focus on optimizing N^+ ion content and interlayer spacing to enhance adsorption efficiency for environmental remediation applications.

Supporting Information

Supporting Information is available from the Wiley Online Library or from the author.

Acknowledgements

J.S.W. and M.Y. contributed equally to this work. The authors thank the National Science and Technology Council (NSTC) of Taiwan (grant no. NSTC 113- 2221-E-005-006) for financial support.

Conflict of Interest

The authors declare no conflict of interest.

Data Availability Statement

The data that support the findings of this study are available from the corresponding author upon reasonable request.

Keywords

adsorption, covalent organic polymers, pyrene, tetraphenylethene, viologen

Received: June 20, 2025
Revised: October 14, 2025
Published online: November 11, 2025

[1] S. Sarkar, A. Chakraborty, P. Nag, S. Singh, R. Munjal, S. R. Vennapusa, H. C. Jha, S. Mukhopadhyay, *ACS Appl. Mater. Interfaces* **2024**, *16*, 62788.
[2] W. Mandal, S. Fajal, S. Mollick, M. M. Shirolkar, Y. D. More, S. Saurabh, D. Mahato, S. K. Ghosh, *ACS Appl. Mate.r Interfaces* **2022**, *14*, 20042.
[3] X. Liu, H. Pang, X. Liu, Q. Li, N. Zhang, L. Mao, X. Liu, H. Pang, X. Liu, Q. Li, N. Zhang, L. Mao, M. Qiu, B. Hu, H. Yang, X. Wang, *Innovation* **2021**, *2*, 100076.
[4] S. Mollick, S. Fajal, S. Saurabh, D. Mahato, S. K. Ghosh, *ACS Cent. Sci.* **2020**, *6*, 1534.
[5] A. Hassan, M. M. R. Mollah, S. Das, N. Das, *J. Mater. Chem. A* **2023**, *11*, 17226.
[6] P. Song, Z. Zhang, L. Yu, P. Wang, Q. Wang, Y. Chen, *New J. Chem.* **2020**, *44*, 8572.
[7] S. J. Olusegun, *Chem. Eng. J.* **2018**, *334*, 1719.
[8] R. Qu, W. Zhang, N. Liu, Q. Zhang, Y. Liu, X. Li, Y. Wei, L. Feng, *ACS Sustain Chem. Eng.* **2018**, *6*, 8019.
[9] C. H. Neoh, Z. Z. Noor, N. S. A. Mutamim, C. K. Lim, *Chem. Eng. J.* **2016**, *283*, 582.
[10] P. Stolzenburg, A. Capdevielle, S. Teychené, B. Biscans, *Chem. Eng. Sci.* **2015**, *133*, 9.
[11] R. He, W. Li, D. Deng, W. Chen, H. Li, C. Wei, Y. Tang, *J. Mater. Chem. A* **2015**, *3*, 9789.
[12] H. Guo, F. You, S. Yu, L. Li, D. Zhao, *J. Memb. Sci.* **2015**, *496*, 310.
[13] L. Goswami, R. V. Kumar, K. Pakshirajan, G. Pugazhenthi, *J. Hazard. Mater.* **2019**, *365*, 707.
[14] L. Rajput, K. Biradha, *J. Mol. Struct.* **2008**, *876*, 339.
[15] Z. Xiang, D. Caob, L. Dai, *Polym. Chem.* **2015**, *6*, 1896.
[16] P. Puthiaraj, Y. R. Lee, S. Zhanga, W. S. Ahn, *J. Mater. Chem. A* **2016**, *4*, 16288.
[17] A. Hassan, N. Das, *ACS Appl. Polym. Mater.* **2023**, *5*, 5349.
[18] S. Fajal, S. Dutta, S. K. Ghosh, *Mater. Horiz.* **2023**, *10*, 4083.
[19] A. Hassan, R. K. Pandey, A. Chakraborty, S. A. Wahed, T. R. Rao, N. Das, *Soft Matter.* **2024**, *20*, 7832.
[20] G. Das, T. Prakasam, S. Nuryyeva, D. S. Han, A. A. Wahab, J. C. Olsen, K. Polychronopoulou, *J. Mater. Chem. A* **2016**, *4*, 15361.
[21] G. Das, T. Skorjanc, S. K. Sharma, F. Gándara, M. Lusi, D. S. S. Rao, S. Vimala, S. K. Prasad, J. Raya, D. S. Han, J. C. Jagannathan, *J. Am. Chem. Soc.* **2017**, *139*, 9558.
[22] G. Das, T. Skorjanc, S. K. Sharma, T. Prakasam, C. P. Iglesias, D. S. Han, J. Raya, J. C. Olsen, R. Jagannathan, A. Trabolsi, *ChemNanoMat* **2018**, *4*, 61.
[23] S. Sarkar, T. Ghosh, A. Chakrobarty, J. Majhi, P. Nag, A. Bandyopadhyay, S. R. Vennapusa, R. Kumar, S. Mukhopadhyay, *ACS Appl. Mater. Interfaces* **2023**, *15*, 28453.
[24] K. Murugavel, *Polym. Chem.* **2014**, *5*, 5873.
[25] X. Xu, H. Chen, N. Huang, *Macromolecules* **2024**, *57*, 9457.
[26] G. Asskar, M. Rivard, T. Martens, *J. Org. Chem.* **2020**, *85*, 1232.
[27] J. Huang, Z. Su, M. Huang, R. Zhang, J. Wang, X. Feng, R. Zhang, R. Zhang, W. Shan, X. Y. Yan, Q. Y. Guo, T. Liu, Y. Liu, Y. Cui, X. Li, A.-C. Shi, S. Z. D. Cheng, *Angew. Chem. Int. Ed.* **2020**, *59*, 18563.
[28] P. Samanta, P. Chandra, S. Dutta, A. V. Desai, S. K. Ghosh, *Chem. Sci.* **2018**, *9*, 7874.
[29] C. Hua, B. Chan, A. Rawal, F. Tuna, D. Collison, J. M. Hook, D. M. D'Alessandro, *J. Mater. Chem. C* **2016**, *4*, 2535.
[30] P. Jhariat, A. Warrier, M. Varghese, T. Panda, *J Mater Chem A Mater* **2025**, *13*, 23893.
[31] G. Kresse, J. Furthmüller, *Mater. Sci.* **1996**, *6*, 15.
[32] G. Kresse, J. Furthmüller, *Phys. Rev. B* **1996**, *54*, 11169.
[33] G. Kresse, J. Furthmüller, *J. Phys. Condens. Matter* **1994**, *6*, 8245.
[34] G. Kresse, D. Joubert, *Phys. Rev. B* **1998**, *59*, 1758.
[35] J. P. Perdew, J. A. Chevary, S. H. Vosko, K. A. Jackson, M. R. Pederson, D. J. Singh, Carlos Fiolhais, *Phys. Rev. B* **1992**, *46*, 6671.
[36] J. Zhao, C. Yang, J. He, L. Liu, J. Yao, Y. Yang, K. Xu, W. Feng, G. Du, L. Zhang, *Int. J. Biol. Macromol.* **2025**, *300*, 140243.
[37] Y. S. Wang, X. Y. Li, R. R. Li, X. N. Yuan, Z. Q. Zhao, X. X. Gou, *RSC Sustainability* **2025**, *3*, 3072.
[38] X. Zhuang, J. Hao, X. Zheng, D. Fu, P. Mo, Y. Jin, P. Chen, H. Liu, G. Liu, W. Lv, *Sep. Purif. Technol.* **2021**, *274*, 118993.
[39] A. Warrier, P. Jhariat, M. Varghese, T. Panda, *Small* **2025**, *21*, e06837.